SCIENCE CHINA Materials ARTICLES

mater.scichina.com link.springer.com

Published online 20 December 2019 | https://doi.org/10.1007/s40843-019-1221-0

Sci China Mater 2020, 63(4): 593–601

Syntheses, characterization, and theoretical calculation of $Rb_2Mg_3(P_2O_7)_2$ polymorphs with deep-ultraviolet cutoff edges

Hongping Wu[1], Shiwei Liu[1], Shichao Cheng[2], Hongwei Yu[1*], Zhanggui Hu[1], Jiyang Wang[1] and Yicheng Wu[1]

ABSTRACT **By the combination of the isolated P_2O_7 dimers and MgO_4 tetrahedra, α- and β-$Rb_2Mg_3(P_2O_7)_2$ polymorphs were synthesized by a high-temperature solution method. α-$Rb_2Mg_3(P_2O_7)_2$ crystallizes in non-centrosymmetric space group $P2_12_12_1$, while β-$Rb_2Mg_3(P_2O_7)_2$ crystallizes in centrosymmetric $P2_1/c$. Both structures contain a three dimensional $[Mg_3P_4O_{14}]^{2-}$ anionic framework, while Rb^+ cations are in the space. Structure analyses show that the isolated P_2O_7 dimers can easily adjust their variable configurations and orientations to fit the different coordination environments of the cations, which is conducive to the formation of polymorphs. The phase transformation process from α- to β-$Rb_2Mg_3(P_2O_7)_2$ was further investigated by powder X-ray diffraction and thermal gravimetric/differential scanning calorimetry measurements. In addition, UV-vis-NIR diffusion spectra indicate both materials have deep-ultraviolet cut-off edges (below 190 nm). α-$Rb_2Mg_3(P_2O_7)_2$ is second-harmonic generation (SHG)-active and the origin of SHG response was investigated by the SHG density calculations. The first-principle calculations were also carried out to illuminate their structure-property relationships.**

Keywords: polymorphs, phosphate, deep-ultraviolet transparent window, structure-property relationship

INTRODUCTION

Nonlinear optical (NLO) materials particularly for ultraviolet (UV) or deep-UV have attracted great concern owing to the ability of expanding the limited laser wavelengths to much wider spectral regions by different frequency conversion. They have been widely used in laser science, photolithography and advanced instrument process [1–16]. Borates possess an absolute advantage for developing UV or deep-UV NLO materials because they have wide optical transparency windows, relatively large second-harmonic generation (SHG) responses and abundant acentric structure units. With several years of sustained exploration and research, many borates with novel crystal structures or excellent optical properties have been reported. Notable examples include a variety of beryllium borates, such as $KBe_2BO_3F_2$ (KBBF) [2], $NH_4Be_2BO_3F_2$ [17], $NaSr_3Be_3B_3O_9F_4$ [18], and some beryllium-free borates, such as $K_3B_6O_{10}Cl$ [19], $Ba_4B_{11}O_{20}F$ [20], and $A_3B_3Li_2M_4B_6O_{20}F$ (A=K, Rb; B=Ba, Sr; M=Al, Ga) [21–25]. Beyond borates, phosphates seem to be a good material system to synthesize the deep-UV NLO materials owing to their short UV cut-off edges, as evidenced by a number of phosphates, such as $BaPO_3Cl$ (180 nm) [26], $Ba_5P_6O_{20}$ (167 nm) [27], and $LiCs_2PO_4$ (147 nm) [28,29]. Besides, phosphates also possess the varied structure characteristics, such as, chains $(PO_3)_\infty$ [30], rings $(P_nO_{3n})^{n-}$ (n = 3, 4, 6, etc.) [31], and isolated groups $(P_nO_{3n+1})^{(n+2)-}$ (n = 1, 2, 3, etc.) [32], which is conducive to synthesizing new phosphates with unique structures [33–36]. For example, $Na_4Mg_3(PO_4)_2P_2O_7$ [33] and $LiMg_3(PO_4)P_2O_7$ [34] exhibit two kinds of isolated P–O groups, $[PO_4]$ and $[P_2O_7]$, in one structure. $Mg_2P_2O_7$ exhibits two different crystal structures ($C2/m$ and $P2_1/c$) both containing isolated P_2O_7 dimers [35], which refer to polymorph that possesses identical chemical composition but different crystal structures, which are fascinating cases for studying the relationship of structure-property and designing new deep-UV NLO materials.

Structural statistics indicate that polymorph phenomenon always exists in orthophosphates and pyrophosphates [37]. Recently, Zhao and co-workers [38] also

[1] Tianjin Key Laboratory of Functional Crystal Materials, Institute of Functional Crystal, Tianjin University of Technology, Tianjin 300384, China
[2] Xinjiang Technical Institute of Physics & Chemistry, Chinese Academy of Sciences, Urumqi 830011, China
* Corresponding author (email: hwyu15@gmail.com)

 © Science China Press and Springer-Verlag GmbH Germany, part of Springer Nature 2019

reported a new deep-UV transparent non-centrosymmetric (NCS) polymorph $RbNaMgP_2O_7$ with isolated P_2O_7 dimers, which contains a new mechanism for the enhancement of the SHG response. In our study, we combine the variable P_2O_7 dimers with the alkali metal and alkali-earth metal cations without d-d or f-f electron transitions, which is beneficial for exploring deep-UV pyrophosphate polymorphs. Through a systematic study, two new pyrophosphate polymorphs, α- and β-$Rb_2Mg_3(P_2O_7)_2$ have been synthesized by a high temperature solution method, in which α-$Rb_2Mg_3(P_2O_7)_2$ crystalizes in NCS space group of $P2_12_12_1$, while β-$Rb_2Mg_3(P_2O_7)_2$ crystalizes in centrosymmetric (CS) space group of $P2_1/c$. Both materials possess deep-UV cutoff edge (<190 nm) and α-$Rb_2Mg_3(P_2O_7)_2$ is SHG-active. In this paper, we report their syntheses, crystal structures, phase transformations, the SHG response and the origin of the SHG response. First-principles calculations were performed to illustrate the relationship between electronic structures and optical properties.

EXPERIMENTAL SECTION

Reagents

Rb_2CO_3 (99%), MgO (99.5%), $NH_4H_2PO_4$ (99%), RbF (99%) were purchased from Aladdin Chemical Co. Ltd. and used as received.

Syntheses

The polycrystalline samples of α- and β-$Rb_2Mg_3(P_2O_7)_2$ were synthesized by the conventional solid-state reaction method. The stoichiometric ratios of Rb_2CO_3 (0.01 mol, 2.31 g), MgO (0.03 mol, 1.20 g) and $NH_4H_2PO_4$ (0.04 mol, 4.60 g) were ground and mixed in an agate mortar. The mixtures were heated at 350°C for 5 h to release the gas of H_2O, CO_2 and NH_3, followed by dwelling at 740°C for α-$Rb_2Mg_3(P_2O_7)_2$ and 840°C for β-$Rb_2Mg_3(P_2O_7)_2$ for 72 h with several grindings to ensure complete reaction. In this way, the pure phases of α- and β-$Rb_2Mg_3(P_2O_7)_2$ polymorphs were obtained.

Crystal growth

Crystals of α- and β-$Rb_2Mg_3(P_2O_7)_2$ were prepared by a high temperature solution method by using the self-flux. They were obtained from a mixture of Rb_2CO_3, MgO and $NH_4H_2PO_4$ in the molar ratio of 3:3:4 for α-$Rb_2Mg_3(P_2O_7)_2$ and 4:3:4 for β-$Rb_2Mg_3(P_2O_7)_2$. The mixtures were melted at 850°C and held at this temperature for 10 h. Then the melt was decreased to 600°C at a rate of 5°C h^{-1} before the furnace was switched off. With these procedures, a few transparent, colorless α- and β-$Rb_2Mg_3(P_2O_7)_2$ crystals were obtained by mechanical separation from the crucible, respectively. The crystals of α- and β-$Rb_2Mg_3(P_2O_7)_2$ are both anti-deliquescent and stable in the air.

X-ray crystallographic studies

The pure phases of α- and β-$Rb_2Mg_3(P_2O_7)_2$ were checked by powder X-ray diffraction (XRD) analyses by using a Rigaku Smartlab 9KW diffractometer equipped with a diffracted beam monochromator set for Cu-Kα radiation (λ = 1.5418 Å). The diffraction patterns use a scan step width of 0.02° and a fixed step rate of 1 s/step with scanning range from 10° to 70° (2θ). The experiment powder XRD patterns of $Rb_2Mg_3(P_2O_7)_2$ polymorphs are in agreement with the calculated ones (Fig. S1).

The crystal structures of $Rb_2Mg_3(P_2O_7)_2$ polymorphs were determined by single-crystal XRD on a Rigaku XtaLAB PRO diffractometer equipped with Mo-Kα (λ = 0.71073 Å) diffracted beam monochromator. The small-sized (several μm in each dimension) single crystal was fixed on thin glass fiber for the data collection. The data were integrated with the SAINT program [39]. The crystal structures were solved by SHELXS-97 and refined on F^2 by a full-matrix least-squares method [40]. The structural symmetry was checked with PLATON [41]. Crystal data and structure refinement information are given in Table 1. Atom coordinates, equivalent isotropic displacement parameters, bond valance sums (BVS), bond lengths and angles for α- and β-$Rb_2Mg_3(P_2O_7)_2$ are listed in Tables S1–S4, respectively.

Thermal analysis

The thermal properties were measured on a NETZSCH STA 449C thermal analyser instrument under flowing N_2. The measurement temperature ranges from 25 to 1000°C for α- and β-$Rb_2Mg_3(P_2O_7)_2$ with a heating rate of 5°C min^{-1}.

UV-vis-NIR and infrared spectra measurements

The diffuse reflectance spectra were measured by a Shimadzu SolidSpec-3700 UV-vis-NIR spectrophotometer with wavelengths ranging from 190 to 2600 nm. The infrared (IR) spectra were investigated by the Shimadzu IRAffinity-1 spectrometer ranging from 400 to 4000 cm^{-1}.

SHG response measurement

The powder SHG responses of α-$Rb_2Mg_3(P_2O_7)_2$ were measured using the Kurtz-Perry method [42] with Q-switched Nd:YAG laser at the wavelength of 1064 nm.

© Science China Press and Springer-Verlag GmbH Germany, part of Springer Nature 2019

Table 1 Crystal data and structure refinement for α- and β-$Rb_2Mg_3(P_2O_7)_2$

Empirical formula	α-$Rb_2Mg_3P_4O_{14}$	β-$Rb_2Mg_3P_4O_{14}$
Formula weight	591.75	591.75
Crystal system space group	Orthorhombic $P2_12_12_1$ (No. 19)	Monoclinic $P2_1/c$ (No. 14)
Unit cell dimensions	a = 9.8458(5) Å	a = 12.9360(8) Å
	b = 10.2972(5) Å	b = 7.3381(5) Å
	c = 13.4520(7) Å	c = 14.7544(9) Å
		β = 90.8010(10)°
Crystal description	Block	Block
Volume (Å^3)	1363.82(12)	1400.43(15)
Z, ρ_{Calcd} (Mg m^{-3})	4, 2.882	4, 2.807
μ (mm^{-1})	7.857	7.652
F(000)	1128	1128
θ range for data collection	2.49° to 25.00°	1.57° to 27.61°
Reflections collected / unique	6727 / 2289 [R(int) = 0.0191]	8500 / 3243 [R(int) = 0.0376]
Completeness to theta	100.00%	99.40%
Refinement method	Full-matrix least-squares on F^2	
Data / restraints / parameters	2289 / 0 / 210	3243 / 0 / 209
GOF on F^2	0.834	1.024
R_1, wR_2[a]	0.0141, 0.0364	0.0331, 0.0676
R_1, wR_2 (all data)	0.0146, 0.0367	0.0460, 0.0728
Flack factor	0.013(4)	N/A
Extinction coefficient	0.0029(2)	0.0032(2)
Largest diff. peak and hole (e Å^{-3})	0.342 and −0.312	0.767 and −0.884

a) $R_1 = \Sigma||F_o| - |F_c||/\Sigma|F_o|$ and $wR_2 = [\Sigma w(F_o^2 - F_c^2)^2 / \Sigma wF_o^4]^{1/2}$ for $F_o^2 > 2\sigma(F_o^2)$

The samples were ground and sieved into distinct particle size ranges (<20, 20–45, 45–63, 63–75, 75–90, 90–125, 125–150 μm). Sieved KH_2PO_4 (KDP) powder was used as a reference.

Calculation method

The electronic structures were calculated using the density functional theory (DFT) implemented in the plane wave pseudopotential method with the CASTEP program [43]. For embodying correlation, core–electron interactions were characterized by norm-conserving pseudopotentials (NCP). Meanwhile, the generalized gradient approximation (GGA) of Perdew–Buker–Ernzerhof (PBE) was exerted to describe the exchange-correlation effects [44–46]. The valence states are as follows: Rb $4s^24p^65s^1$, Cs $5s^25p^66s^1$, Mg $4s^24p^65s^1$, P $3s^23p^3$, and O $2s^22p^4$. To achieve energy convergence, the plane-wave basis energy cutoff values were set at 990 eV for $Rb_2Mg_3(P_2O_7)_2$ polymorphs. Monkhorst-pack k-point used in sampling was 1 × 2 × 1.

RESULTS AND DISCUSSION

Crystal structures of α- and β-$Rb_2Mg_3(P_2O_7)_2$

α-$Rb_2Mg_3(P_2O_7)_2$ crystallizes in the orthorhombic crystal system with the NCS space group $P2_12_12_1$ (No. 19), while β-$Rb_2Mg_3(P_2O_7)_2$ crystallizes in monoclinic crystal system with a CS space group, $P2_1/c$ (No. 14). Their asymmetric units both contain two crystallographically independent Rb atoms, four P atoms, three Mg atoms and fourteen O atoms. All atoms stay at the Wyckoff positions 4a for α-$Rb_2Mg_3(P_2O_7)_2$ and 4e for β-$Rb_2Mg_3(P_2O_7)_2$ (Tables S1 and S2). In both structures, all P atoms exhibit typical tetrahedrally coordinated environment with the P–O bond distances ranging from 1.4859(19) to 1.6336(19) Å and all Mg atoms connect with oxygen atoms to form MgO_4 tetrahedra with the Mg–O bond distances ranging from 1.905(2) to 2.0427(19) Å. It is worth noting that in the two structures, the PO_4 tetrahedron connects with each other to form two types of P_2O_7 dimers from four crystallographically independent P atoms.

 © Science China Press and Springer-Verlag GmbH Germany, part of Springer Nature 2019

The ball-and-stick representations of the structures for α- and β-$Rb_2Mg_3(P_2O_7)_2$ are shown in Figs 1 and 2, respectively. In their structures, each P_2O_7 dimer shares its six vertices with six MgO_4 tetrahedra, likewise, each MgO_4 tetrahedron is linked with four different P_2O_7 dimers through its terminal O atoms to form the $[Mg_3(P_2O_7)_2]_\infty$ frameworks with Rb^+ cations filled in the space of frameworks. In α-$Rb_2Mg_3(P_2O_7)_2$, the isolated MgO_4 tetrahedra and P_2O_7 dimers are related by the 2_1-screw axes along *a*, *b* and *c*-axes and Rb^+ cations exhibit two coordination environments, i.e., $Rb(1)O_9$ and $Rb(2)O_{11}$ with Rb–O bond lengths ranging from 2.928(2) to 3.559(2) Å. The $Rb(1)O_9$ polyhedra share faces with $Rb(2)O_{11}$ polyhedra to form a three dimensional (3D) framework (Fig. S2). Bond valence calculations result in BVS of 1.01 and 1.03 for the Rb^+ cations, 4.84–4.90 for the P^{5+} cations, 2.04–2.12 for the Mg^{2+} cations, 1.86–2.19 for the O^{2-} anions (Table S1). In β-$Rb_2Mg_3(P_2O_7)_2$, the isolated MgO_4 tetrahedra and P_2O_7 dimers are operated by the *c*-glide plane perpendicular to *b* direction and 2_1 screw axis along *b* direction exhibiting an inversion centre. The Rb^+ cations also exhibit two coordination environments, $Rb(1)O_8$ and $Rb(2)O_{10}$.

For the $Rb(1)O_8$ and $Rb(2)O_{10}$, they firstly share edges to form $Rb(1)_2O_{14}$ dimers and $Rb(2)_2O_{18}$ dimers, and further these $Rb(1)_2O_{14}$ dimers and $Rb(2)_2O_{18}$ dimers are alternately connected to construct 2D layers (Fig. S3), with the Rb–O distances in the range of 2.825(1)–3.559(2) Å. Bond valence calculations result in values of 0.87 and 0.91 for the Rb^+ cations, 5.03–5.09 for the P^{5+} cations, 2.08–2.16 for the Mg^{2+} cations, 1.91–2.14 for the O^{2-} anions (Table S2). The bond lengths in these two structures are comparable to those of other reported compounds [47,48].

As described above, α- and β-$Rb_2Mg_3(P_2O_7)_2$ show the similar anionic frameworks, which are both constructed by the P_2O_7 dimers and MgO_4 tetrahedra through corner-sharing. It provides the possibility for their phase transformation. However, some obvious differences between them can also be observed. In order to show their differences more clearly, their structures were analyzed based on the topological point of view. The P_2O_7 dimers and MgO_4 tetrahedra are regarded as 6-connected nodes and 4-connected nodes, respectively. The topological structures for α- and β-$Rb_2Mg_3(P_2O_7)_2$ are shown in Fig. 3. Clearly, in α-$Rb_2Mg_3(P_2O_7)_2$, two different types of P_2O_7 dimers and the MgO_4 tetrahedra are interweaved with each other to form 3D frameworks. While in β-$Rb_2Mg_3(P_2O_7)_2$, two different types of P_2O_7 dimers and MgO_4 tetrahedra are alternatively stacked along *a*-axis,

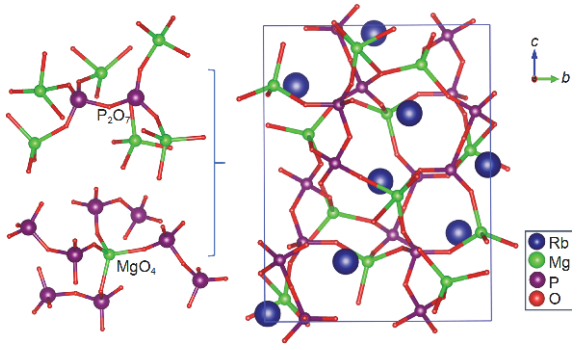

Figure 1 Ball-and-stick representation of α-$Rb_2Mg_3(P_2O_7)_2$. All of the Rb–O bonds are omitted for clarity.

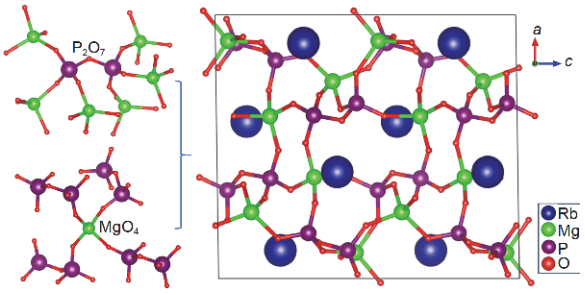

Figure 2 Ball-and-stick representation of β-$Rb_2Mg_3(P_2O_7)_2$. All of the Rb–O bonds are omitted for clarity.

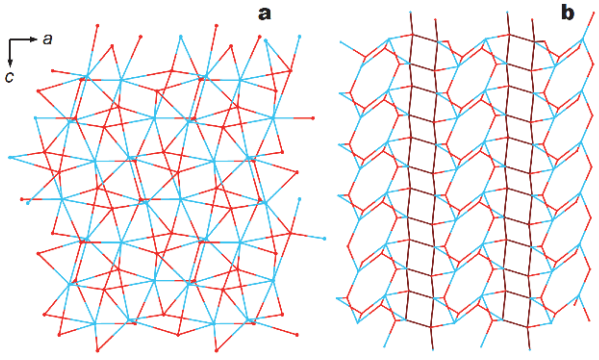

Figure 3 The "Connection" mode of P_2O_7 dimers and MgO_4 tetrahedra in the structures of α-$Rb_2Mg_3(P_2O_7)_2$ (a) and β-$Rb_2Mg_3(P_2O_7)_2$ (b) (P_2O_7 dimer as a blue node; MgO_4 tetrahadron as a dark red node).

forming the so-called sandwich type. These great different structure frameworks between α- and β-$Rb_2Mg_3(P_2O_7)_2$ seem to suggest a quite large energy-barrier for their phase transformation. Furthermore, the Madelung energies of α- to β-$Rb_2Mg_3(P_2O_7)_2$ were calculated with Fourier method by using an external program MADEL embedded in the VESTA program [49]. The Madelung energies for α- and β-$Rb_2Mg_3(P_2O_7)_2$ are −106.026 and

© Science China Press and Springer-Verlag GmbH Germany, part of Springer Nature 2019

−106.0344 (×10^3 KJ mol^{-1}), which are close to each other, favoring their phase transformation.

More detailedly, we compared the configurations of P_2O_7 and MgO_4 tetrahedra in the two compounds. In fact, the Mg(1)O_4 can be seen as Mg(1)O_{4+1} considering the longer Mg–O bond lengths (2.2492(19) Å) in α-$Rb_2Mg_3(P_2O_7)_2$. In other words, we can observe Mg(1)O_5 and Mg(2, 3)O_4 groups in α-$Rb_2Mg_3(P_2O_7)_2$ (Fig. S4). However, with the thermo-induced volume expansion, the longest Mg–O bonds (2.249 Å) are easy to break owing to weak bond strength. Thus, in β-$Rb_2Mg_3(P_2O_7)_2$, we only observe one coordinated environment Mg atoms, isolated MgO_4 tetrahedra with the Mg–O bond distances ranging from 1.908(3) to 1.951(3) Å. In addition, two different types of P_2O_7 dimers are distinguished by their bond lengths and the dihedral angles of two PO_4 tetrahedra (Fig. 4). The bond angles of P(2)–O(1)–P(1) and P(3)–O(8)–P(4) are 133.39° and 127.83° in α-$Rb_2Mg_3(P_2O_7)_2$, while, the bond angles of P(2)–O(2)–P(1) and P(3)–O(1)–P(4) are 131.10° and 132.91° in β-$Rb_2Mg_3(P_2O_7)_2$. And the symmetry of isolated P_2O_7 dimers has been changed from 2_1 screw axes along *a, b* and *c* axes in α-$Rb_2Mg_3(P_2O_7)_2$ to the *c*-glide plane perpendicular to *b* direction and 2_1 screw axis along *b* direction in β-$Rb_2Mg_3(P_2O_7)_2$ (Fig. 4). These suggest that the different types of P_2O_7 dimers can be easily modified only through a small change of P–O bond lengths and P–O–P bond angles to fit different coordination environments of Rb^+ cation, which is conducive to the phase transformation between α- and β-$Rb_2Mg_3(P_2O_7)_2$ polymorphs.

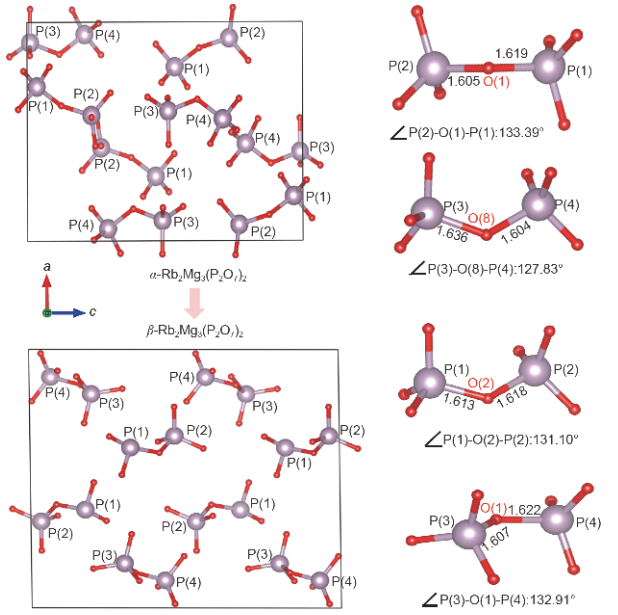

Figure 4 The arrangement and the distortion of P_2O_7 dimers in α- and β-$Rb_2Mg_3(P_2O_7)_2$.

Polymorphism and phase transformation of α- to β-$Rb_2Mg_3(P_2O_7)_2$

To investigate the phase transformation from α- to β-$Rb_2Mg_3(P_2O_7)_2$, the solid-state reactions at different temperatures were carried out and the thermogravimetric analysis/differential scanning calorimetry (TG/DSC) of α-$Rb_2Mg_3(P_2O_7)_2$ was conducted. Firstly, the pure polycrystalline samples of α- and β-$Rb_2Mg_3(P_2O_7)_2$ were synthesized by the traditional solid-state reaction technique at different temperatures, 740°C for α-$Rb_2Mg_3(P_2O_7)_2$ and 840°C for β-$Rb_2Mg_3(P_2O_7)_2$. The phase purity of the samples was confirmed by powder XRD patterns (Fig. 5). Further, a series of solid state reactions were also carried out from 780 to 820°C and their powder XRD patterns are also shown in Fig. 5. Clearly, the powder

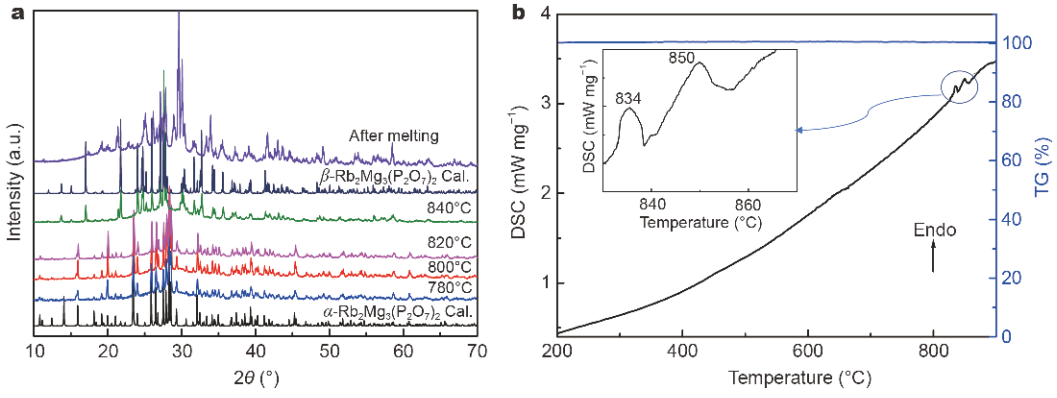

Figure 5 (a) The powder XRD patterns of $Rb_2Mg_3(P_2O_7)_2$ at different temperatures; (b) TG and DSC curves of α-$Rb_2Mg_3(P_2O_7)_2$ (TG curve is represented by the blue line, and DSC curve is represented by the black line).

© Science China Press and Springer-Verlag GmbH Germany, part of Springer Nature 2019

XRD patterns from 780 to 820°C agree well with α-$Rb_2Mg_3(P_2O_7)_2$. While, a higher temperature, 840°C, will lead to the generation of β-$Rb_2Mg_3(P_2O_7)_2$, which suggests that the phase transformation temperature is around 840°C. Furthermore, the isothermal annealing experiment of β-$Rb_2Mg_3(P_2O_7)_2$ was also performed at 780°C, which is in the stable temperature range of α-$Rb_2Mg_3(P_2O_7)_2$. It proves that the phase transformation from α- to β-$Rb_2Mg_3(P_2O_7)_2$ is irreversible. The TG/DSC curves are shown in Fig. 5 and two endothermic peaks are observed on the DSC heating curve at 834 and 850°C, respectively. There is no obvious weight loss on the TG curve. The powder XRD analysis shows the residues after TG/DSC are mainly $Mg_2P_2O_7$ (PDF32-0626, Fig. S5). Thus, the two endothermic peaks on the DSC curve should correspond to the phase transformation from α- to β-$Rb_2Mg_3(P_2O_7)_2$ (834°C) and the incongruently melting of β-Rb_2Mg_3-$(P_2O_7)_2$ (850°C).

IR and UV-vis-NIR spectra

The IR spectra of α- and β-$Rb_2Mg_3(P_2O_7)_2$ are shown in Fig. S6. They exhibit similar absorption characteristics. The peaks around 1118 cm^{-1} can be assigned to the stretching vibrations of ν_s(O–P–O) [50]. The peaks near 947 cm^{-1} are caused by ν_{as}(P–O–P) and ν_s(P–O–P). The peaks around 727 and 610 cm^{-1} belong to ν_s(P–O–P) [51]. The peaks at 552 and 450 cm^{-1} can be assigned to the stretching vibrations of δ_{as}(P–O–P) and δ_s(P–O–P) [52], respectively. These characteristic peaks prove the existence of the PO_4 tetrahedra, which is consistent with other reported phosphates.

The UV-vis-NIR diffuse reflectance spectra for the two compounds are shown in Fig. S7. They indicate that the two compounds possess short UV cutoff edges (shorter than 190 nm). Based on the Kubelka–Munk function, the band gaps calculated for α- and β-$Rb_2Mg_3(P_2O_7)_2$ are 5.74 and 5.65 eV, respectively (Fig. S7).

SHG response

Since α-$Rb_2Mg_3(P_2O_7)_2$ crystallizes in the NCS space group, its SHG response was also measured. It reveals that α-$Rb_2Mg_3(P_2O_7)_2$ is SHG-active. Its SHG response is around 0.2 × KDP and it is phase-matchable (Fig. S8). The value is comparable to other reported deep-UV NLO phosphates, such as $Rb_2Ba_3(P_2O_7)_2$ (0.3 × KDP), $Ba_3P_3O_{10}Cl$ (0.6 × KDP), and $Ba_5P_6O_{10}$ (0.8 × KDP).

Electronic structure calculations

The band structures of α- and β-$Rb_2Mg_3(P_2O_7)_2$ were calculated for a better understanding of the relationship between electronic structures and optical properties. α- and β-$Rb_2Mg_3(P_2O_7)_2$ exhibit the similar band structures and they are both indirect band gap compounds with the band gaps of 4.98 and 4.87 eV for α- and β-Rb_2Mg_3-$(P_2O_7)_2$, respectively. The calculated band gaps are a little smaller than experimental ones. That can be attributed to the insufficient accuracy of the exchange correlation energy. In order to adjust the differences based on DFT band structure calculation results, the scissors shifts, 0.76 and 0.78 eV were used for calculating the optical properties. The calculated density of states (DOS) and partial DOS (PDOS) are shown in Fig. 6. For both materials, the top of valence bands (VBs) near the Fermi level from −3 to 0 eV are mainly composed of the 2p orbitals of oxygen atoms and 3p orbitals of phosphorus, while the bottom of conduction band (CB) region is mostly composed of the hybridization orbitals of Rb and Mg atoms, and the Rb atoms have the major contribution. These indicate that the observed absorptions on their diffuse reflectance spectra mainly originate from the charge transfer from the O 2p states to the Rb 5s states.

In addition, the SHG coefficients of α-$Rb_2Mg_3(P_2O_7)_2$ was also calculated. α-$Rb_2Mg_3(P_2O_7)_2$ belongs to point group 222 and has only one independent nonvanishing second-order NLO susceptibility tensor d_{14}, under the restriction of Kleinman's symmetry. The calculated value for d_{14} is −0.22 pm V^{-1}, approximately 0.6 × KDP (d_{36}KDP = 0.39 pm V^{-1}), which is consistent with the experimental SHG intensity. To investigate the contribution of each atom for SHG response, the SHG-densities of α-$Rb_2Mg_3(P_2O_7)_2$ were calculated and shown in Fig. 7. The SHG process can be described by two virtual transition processes, namely virtual electron (VE) and virtual hole (VH) processes, which have the main contribution to the SHG coefficients. So we display the unoccupied and occupied states of the VE process. In the unoccupied states, the SHG densities are mainly accumulated on O and P, and few are accumulated on Mg atoms. While in the occupied states, the O atoms are dominant. Therefore, the SHG effect of α-$Rb_2Mg_3(P_2O_7)_2$ may come from the synergistic effects of the P–O and Mg–O groups.

CONCLUSIONS

Two new polymorphic phosphates, α- and β-Rb_2Mg_3-$(P_2O_7)_2$ have been synthesized through a high-temperature solution method. Their structure frameworks are both composed of P_2O_7 dimers and MgO_4 tetrahdra, and the connection modes between P_2O_7 dimers and MgO_4 tetrahdra are very similar, i.e., each P_2O_7 dimer connects

 © Science China Press and Springer-Verlag GmbH Germany, part of Springer Nature 2019

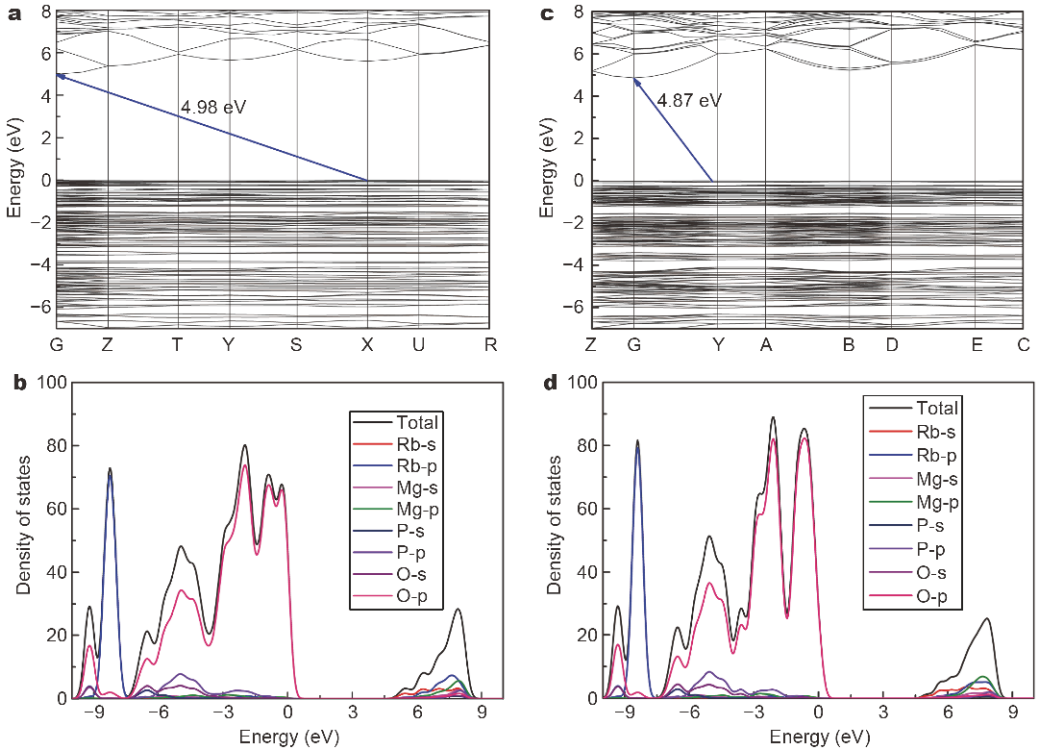

Figure 6 The calculated band structures and the total and partial densities of states of α-$Rb_2Mg_3(P_2O_7)_2$ (a, b); β-$Rb_2Mg_3(P_2O_7)_2$ (c, d).

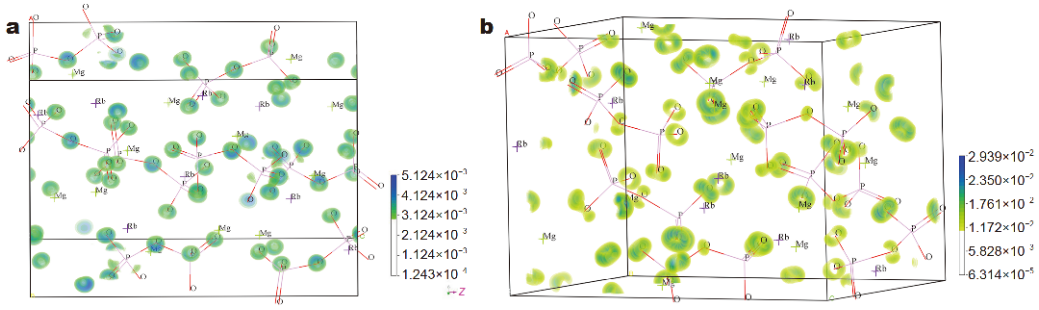

Figure 7 The SHG-density of unoccupied (a) and occupied (b) states of α-$Rb_2Mg_3(P_2O_7)_2$ in the VE process.

with six MgO_4 tetrahdra, likewise each MgO_4 tetrahdron connects with four P_2O_7 dimers. This provides the possibility for their phase-transformation. Furthermore, the solid state reactions at different temperatures and the TG/DSC measurement suggest that the phase-transformation from α- to β-$Rb_2Mg_3(P_2O_7)_2$ happens around 834°C and it is irreversible. The calculated Madelung energy shows that α- to β-$Rb_2Mg_3(P_2O_7)_2$ are both thermally stable, and both compounds have short UV cutoff edges (<190 nm). First-principle calculations indicate that the band gaps of α- and β-$Rb_2Mg_3(P_2O_7)_2$ are determined by the charge transfer from O 2p orbitals to Rb 5s orbitals, and the SHG response of α-$Rb_2Mg_3(P_2O_7)_2$ mainly originates from the P–O and Mg–O tetrahedra. The syntheses for other deep-UV NLO phospates are still on the way.

Received 29 October 2019; accepted 19 November 2019; published online 20 December 2019

1 Becker P. Borate materials in nonlinear optics. Adv Mater, 1998, 10: 979–992
2 Cheng Y, Liu XJ. Three dimensional multilayered acoustic cloak with homogeneous isotropic materials. Appl Phys A, 2009, 94: 25–30
3 Cyranoski D. Materials science: China's crystal cache. Nature, 2009, 457: 953–955

 © Science China Press and Springer-Verlag GmbH Germany, part of Springer Nature 2019

4 Chen CT, Wu BC, Jiang AD, *et al.* A new-type ultraviolet SHG crystal—β-BaB_2O_4. Sci Sin B, 1985, 28:235–243
5 Chen C, Wu Y, Jiang A, *et al.* New nonlinear-optical crystal: LiB_3O_5. J Opt Soc Am B, 1989, 6: 616–621
6 Liang F, Kang L, Lin Z, *et al.* Analysis and prediction of mid-IR nonlinear optical metal sulfides with diamond-like structures. Coord Chem Rev, 2017, 333: 57–70
7 Tran TT, Yu H, Rondinelli JM, *et al.* Deep ultraviolet nonlinear optical materials. Chem Mater, 2016, 28: 5238–5258
8 Wang XX, Li XB, Hu CL, *et al.* $Ag_4Hg(SeO_3)_2(SeO_4)$: a novel SHG material created in mixed valent selenium oxides by *in situ* synthesis. Sci China Mater, 2019, 62: 1821–1830
9 Xie Z, Wang Y, Cheng S, *et al.* Synthesis, characterization, and theoretical analysis of three new nonlinear optical materials $K_7MRE_2B_{15}O_{30}$ (M= Ca and Ba, RE= La and Bi). Sci China Mater, 2019, 62: 1151–1161
10 Yang Y, Gong P, Huang Q, *et al.* $KNa_4B_2P_3O_{13}$: A deep-ultraviolet transparent borophosphate exhibiting second-harmonic generation response. Inorg Chem, 2019, 58: 8918–8921
11 Mutailipu M, Zhang M, Zhang B, *et al.* $SrB_5O_7F_3$ functionalized with $[B_5O_9F_3]^{6-}$ chromophores: Accelerating the rational design of deep-ultraviolet nonlinear optical materials. Angew Chem Int Ed, 2018, 57: 6095–6099
12 Shi G, Wang Y, Zhang F, *et al.* Finding the next deep-ultraviolet nonlinear optical material: $NH_4B_4O_6F$. J Am Chem Soc, 2017, 139: 10645–10648
13 Huang J, Guo S, Zhang Z, *et al.* Designing excellent mid-infrared nonlinear optical materials with fluorooxo-functional group of d^0 transition metal oxyfluorides. Sci China Mater, 2019, 62: 1798–1806
14 Wang Y, Zhang B, Yang Z, *et al.* Cation-tuned synthesis of fluorooxoborates: towards optimal deep-ultraviolet nonlinear optical materials. Angew Chem Int Ed, 2018, 57: 2150–2154
15 Chen CT, Sasaki T, Li RK, *et al.* Nonlinear Optical Borate Crystals: Principles and Applications. Weinheim: Wiley-VCH, 2012
16 Luo M, Liang F, Song Y, *et al.* $M_2B_{10}O_{14}F_6$ (M = Ca, Sr): Two noncentrosymmetric alkaline earth fluorooxoborates as promising next-generation deep-ultraviolet nonlinear optical materials. J Am Chem Soc, 2018, 140: 3884–3887
17 Peng G, Ye N, Lin Z, *et al.* $NH_4Be_2BO_3F_2$ and γ-Be_2BO_3F: Overcoming the layering habit in $KBe_2BO_3F_2$ for the next-generation deep-ultraviolet nonlinear optical materials. Angew Chem Int Ed, 2018, 57: 8968–8972
18 Huang H, Yao J, Lin Z, *et al.* $NaSr_3Be_3B_3O_9F_4$: A promising deep-ultraviolet nonlinear optical material resulting from the cooperative alignment of the $[Be_3B_3O_{12}F]^{10-}$ anionic group. Angew Chem Int Ed, 2011, 50: 9141–9144
19 Wu H, Pan S, Poeppelmeier KR, *et al.* $K_3B_6O_{10}Cl$: A new structure analogous to perovskite with a large second harmonic generation response and deep UV absorption edge. J Am Chem Soc, 2011, 133: 7786–7790
20 Wu H, Yu H, Yang Z, *et al.* Designing a deep-ultraviolet nonlinear optical material with a large second harmonic generation response. J Am Chem Soc, 2013, 135: 4215–4218
21 Zhao S, Kang L, Shen Y, *et al.* Designing a beryllium-free deep-ultraviolet nonlinear optical material without a structural instability problem. J Am Chem Soc, 2016, 138: 2961–2964
22 Wu H, Yu H, Pan S, *et al.* Deep-ultraviolet nonlinear-optical material $K_3Sr_3Li_2Al_4B_6O_{20}F$: Addressing the structural instability problem in $KBe_2BO_3F_2$. Inorg Chem, 2017, 56: 8755–8758
23 Yu H, Young J, Wu H, *et al.* The next-generation of nonlinear optical materials: $Rb_3Ba_3Li_2Al_4B_6O_{20}F$—synthesis, characterization, and crystal growth. Adv Opt Mater, 2017, 5: 1700840
24 Shen Y, Zhao S, Yang Y, *et al.* A new KBBF-family nonlinear optical material with strong interlayer bonding. Cryst Growth Des, 2017, 17: 4422–4427
25 Meng X, Liang F, Xia M, *et al.* Beryllium-free nonlinear-optical crystals $A_3Ba_3Li_2Ga_4B_6O_{20}F$ (A = K and Rb): Members of the $Sr_2Be_2(BO_3)_2O$ family with a strong covalent connection between the $_\infty^2[Li_2Ga_4B_6O_{20}F]^{9-}$ double layers. Inorg Chem, 2018, 57: 5669–5676
26 Yu P, Wu LM, Zhou LJ, *et al.* Deep-ultraviolet nonlinear optical crystals: $Ba_3P_3O_{10}X$ (X = Cl, Br). J Am Chem Soc, 2014, 136: 480–487
27 Zhao S, Gong P, Luo S, *et al.* Tailored synthesis of a nonlinear optical phosphate with a short absorption edge. Angew Chem Int Ed, 2015, 54: 4217–4221
28 Li L, Wang Y, Lei BH, *et al.* A new deep-ultraviolet transparent orthophosphate $LiCs_2PO_4$ with large second harmonic generation response. J Am Chem Soc, 2016, 138: 9101–9104
29 Shen Y, Yang Y, Zhao S, *et al.* Deep-ultraviolet transparent Cs_2LiPO_4 exhibits an unprecedented second harmonic generation. Chem Mater, 2016, 28: 7110–7116
30 Sun T, Shan P, Chen H, *et al.* Growth and properties of a non-centrosymmetric polyphosphate $CsLa(PO_3)_4$ crystal with deep-ultraviolet transparency. CrystEngComm, 2014, 16: 10497–10504
31 Belharouak I, Aouad H, Mesnaoui M, *et al.* Crystal structure and luminescence properties of silver in $AgM(PO_3)_3$ (M=Mg, Zn, Ba) polyphosphates. J Solid State Chem, 1999, 145: 97–103
32 Trad K, Carlier D, Croguennec L, *et al.* A layered iron(III) phosphate phase, $Na_3Fe_3(PO_4)_4$: Synthesis, structure, and electrochemical properties as positive electrode in sodium batteries. J Phys Chem C, 2010, 114: 10034–10044
33 Essehli R, El Bali B, Benmokhtar S, *et al.* Synthesis, crystal structure and infrared spectroscopy of a new non-centrosymmetric mixed-anion phosphate $Na_4Mg_3(PO_4)_2(P_2O_7)$. J Alloys Compd, 2010, 493: 654–660
34 Kim SC, Lee MS, Kang J, *et al.* Crystal structure and ion conductivity of a new mixed-anion phosphate $LiMg_3(PO_4)P_2O_7$. J Solid State Chem, 2015, 225: 335–339
35 Durif A. Crystal Chemistry of Condensed Phosphates. New York: Plenum Press, 1995
36 Yu H, Young J, Wu H, *et al.* $M_4Mg_4(P_2O_7)_3$ (M = K, Rb): Structural engineering of pyrophosphates for nonlinear optical applications. Chem Mater, 2017, 29: 1845–1855
37 Dunitz JD, Bernstein J. Disappearing polymorphs. Acc Chem Res, 1995, 28: 193–200
38 Zhao S, Yang X, Yang Y, *et al.* Non-centrosymmetric $RbNaMgP_2O_7$ with unprecedented thermo-induced enhancement of second harmonic generation. J Am Chem Soc, 2018, 140: 1592–1595
39 Inc Madison WI. Bruker, Analytical X-ray Instruments, SAINT, version 7.60A, 2008
40 Sheldrick GM. SHELXTL, version 6.14. Bruker analytical X ray instruments, Inc., Madison, WI, 2003
41 Spek AL. Single-crystal structure validation with the program *PLATON*. J Appl Crystlogr, 2003, 36: 7–13
42 Kurtz SK, Perry TT. A powder technique for the evaluation of nonlinear optical materials. J Appl Phys, 1968, 39: 3798–3813
43 Clark SJ, Segall MD, Pickard CJ, *et al.* First principles methods

 © Science China Press and Springer-Verlag GmbH Germany, part of Springer Nature 2019

using CASTEP. Z für Kristallographie - Crystline Mater, 2005, 220: 567–570
44 Perdew JP, Burke K, Ernzerhof M. Generalized gradient approximation made simple. Phys Rev Lett, 1996, 77: 3865–3868
45 Rappe AM, Rabe KM, Kaxiras E, *et al.* Optimized pseudopotentials. Phys Rev B, 1990, 41: 1227–1230
46 Lin JS, Qteish A, Payne MC, *et al.* Optimized and transferable nonlocal separable *ab initio* pseudopotentials. Phys Rev B, 1993, 47: 4174–4180
47 Lu X, Wu R, Jing Q, *et al.* Non-centrosymmetric $BaNaP_3O_9$ with a short deep-ultraviolet cutoff edge. J Alloys Compd, 2018, 764: 170–176
48 Chen YG, Xing ML, Liu PF, *et al.* Two phosphates: non-centrosymmetric $Cs_6Mg_6(PO_3)_{18}$ and centrosymmetric $Cs_2MgZn_2(P_2O_7)_2$. Inorg Chem, 2017, 56: 845–851
49 Harris FE, Monkhorst HJ. Electronic-structure studies of solids. I. fourier representation method for madelung sums. Phys Rev B, 1970, 2: 4400–4405
50 Nyquist RA, Kagel RO. Infrared Spectra of Inorganic Compounds (3800–45 cm^{-2}). New York: Academic press, 1971
51 Abudoureheman M, Han S, Wang Y, *et al.* $A_3Sr_2P_7O_{21}$ (A = Rb, Cs): Two polyphosphates based on different types of P–O chains and ring structures. Inorg Chem, 2017, 56: 3939–3945
52 Chen Z, Fang Y, Zhang W, *et al.* $ALiZnP_2O_7$ (A = Rb, Cs): Two mixed alkali zinc pyrophosphates featuring a $[Li_2Zn_2P_4O_{20}]^{14-}$ anionic skeleton. Inorg Chem, 2018, 57: 10568–10575

Acknowledgements This work was financially supported by the National Natural Science Foundation of China (51972230, 51802217, 61835014, 51890864 and 51890865), the Natural Science Foundation of Tianjin (19JCZDJC38200), and the National Key Research and Development Project (2016YFB0402103).

Author contributions Wu H, and Liu S performed the experiments, data analysis, and paper writing; Cheng S performed the theoretical data analysis; Yu H, Hu Z, Wang J and Wu Y designed the concept and supervised the experiments. All authors contributed to the general discussion.

Conflict of interest The authors declare that they have no conflict of interest.

Supplementary information The supporting data are available in the online version of the paper. Accession Codes: CCDC 1947460 and 1947461 contain the supplementary crystallographic data for this paper. These data can be obtained free of charge *via* www.ccdc.cam.ac.uk/data_request/cif, or by emailing data_request@ccdc.cam.ac.uk, or by contacting The Cambridge Crystallographic Data Centre, 12 Union Road, Cambridge CB2 1EZ, UK; fax: +441223 336033.

Hongping Wu received her PhD in 2012 from Xinjiang University. In the same year, she started her independent career as an associate professor at Xinjiang Technical Institute of Physics & Chemistry of CAS (XTIPC, CAS). In 2017, she was promoted to a full professor at XTIPC. From 2018, she has been working as a full professor at Tianjin University of Technology. Her current research interest focuses on new NLO materials.

Hongwei Yu received his PhD degree in material physics and chemistry from University of Chinese Academy of Sciences under the direction of Professor Shilie Pan. He did post-doctoral research at Houston University and Northwestern University in USA from 2014 to 2017. From 2018, he has been working as a full professor at Tianjin University of Technology. His current research interests include the design, synthesis, crystal growth, and evaluation of new optical electronic functional materials.

拥有深紫外截止边的$Rb_2Mg_3(P_2O_7)_2$同质多晶的合成、表征和理论计算

吴红萍[1], 刘世伟[1], 程世超[2], 俞洪伟[1*], 胡章贵[1], 王继扬[1], 吴以成[1]

摘要 本文结合孤立的P_2O_7二聚体和MgO_4四面体，采用高温熔液法合成了α和β-$Rb_2Mg_3(P_2O_7)_2$同质多晶. α-$Rb_2Mg_3(P_2O_7)_2$结晶于非中心对称$P2_12_12_1$空间群，β-$Rb_2Mg_3(P_2O_7)_2$结晶于中心对称$P2_1/c$空间群. 两种结构均含有三维$[Mg_3P_4O_{14}]^{2-}$阴离子骨架，而Rb^+离子位于空间中. 结构分析表明，孤立的P_2O_7通过调整其可变构型和取向以适合不同配位环境的阳离子，这有利于同质多晶$Rb_2Mg_3(P_2O_7)_2$的形成. 另外，从α-到β-$Rb_2Mg_3(P_2O_7)_2$的相转变过程也可以通过粉末X射线衍射和热重-差热测试被进一步证明. 紫外-可见-近红外漫反射光谱测试表明两种材料都有深紫外截止边(190 nm以下)，并且α-$Rb_2Mg_3(P_2O_7)_2$具有倍频效应，我们通过倍频密度计算研究了其倍频效应的来源. 为了更好地理解上述化合物的结构性能关系，我们还进行了第一性原理计算.

 © Science China Press and Springer-Verlag GmbH Germany, part of Springer Nature 2019